CRYSTAL GROWTH & DESIGN

Article

Cite This: Cryst. Growth Des. 2019, 19, 2765−2771

pubs.acs.org/crystal

Nonstoichiometry Driven Ferromagnetism in Double Perovskite $La_2Ni_{1-x}Mn_{1+x}O_6$ Insulating Thin Films

Monica Bernal-Salamanca,[*,†] Zorica Konstantinović,[†,‡] Lluis Balcells,[†] Elisa Pannunzio-Miner,[†,§] Felip Sandiumenge,[†] Laura Lopez-Mir,[†] Bernat Bozzo,[†] Javier Herrero-Martín,[⊥] Alberto Pomar,[†] Carlos Frontera,[†] and Benjamín Martínez[†]

[†]Institut de Ciència de Materials de Barcelona, ICMAB-CSIC, Campus UAB, 08193 Bellaterra, Spain

[‡]Center for Solid State Physics and New Materials, Institute of Physics Belgrade, University of Belgrade, Pregrevica 118, 11080 Belgrade, Serbia

[§]Facultad de Ciencias Exactas, Físicas y Naturales, Centro de Investigaciones en Ciencias de la Tierra (CICTERRA-CONICET-UNC), Av. Velez Sarfield 1611, X5016GCA Ciudad Universitaria, Cordoba, Argentina

[⊥]ALBA Synchrotron Light Source, C. de la Llum 2-26, E 08920 Cerdanyola del Vallès, Spain

Supporting Information

ABSTRACT: In this work we report on the epitaxial growth of La_2NiMnO_6 double perovskite thin films on top of (001) oriented $SrTiO_3$ substrates by RF magnetron sputtering. The influence of oxygen pressure (P_{O_2}) and growth temperature on the microstructure, stoichiometry of the films, and magnetic and transport properties is thoroughly investigated. It is found that high oxygen pressure promotes the growth of stoichiometric films, with a Ni/Mn ratio almost equal to 1. However, these films exhibit poor ferromagnetic properties with respect to the expected optimum values corresponding to ferromagnetic ordering mediated by superexchange interaction between Mn^{4+} and Ni^{2+} according to the Goodenough-Kanamori rules. Most interestingly, films grown at low P_{O_2} exhibit Ni/Mn ratios below 1, but ferromagnetic properties close to the optimal ones. The valence balance between Ni and Mn ions in nonstoichiometric sample has been elucidated by X-ray absorption spectroscopy. The results indicate that Ni deficiency plays a crucial role in the puzzling insulating ferromagnetic behavior observed in nonstoichiometric samples.

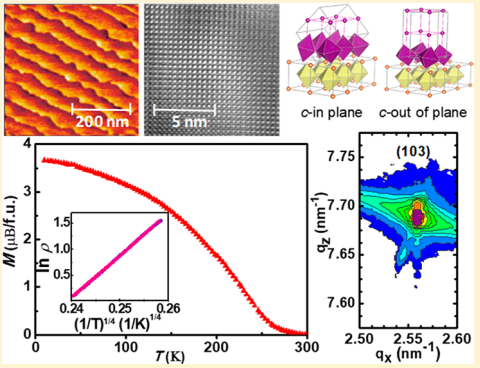

INTRODUCTION

The urgent need to solve the problems of energetic efficiency and data storage and processing speed of current microelectronic devices has boosted the search for new materials and paradigms capable of circumventing those problems. Spintronics has been signaled as a potential alternative technology to develop multifunctional electronics that combines logic operations, data storage and transmission with an improved energetic efficiency. The development of spintronic devices requires the generation and control of highly spin-polarized currents[1] or pure spin currents.[2] A way of obtaining a highly spin polarized current is by using a spin filtering effect through ferromagnetic-insulator-ferromagnetic tunnel barriers.[3,4] The same effect can be obtained simply by using a ferromagnetic insulating barrier.[5,6] However, ferromagnetic insulators (FMI) are very scarce; among the few FMI known double perovskite (DP) oxides, like La_2NiMnO_6 (LNMO) and La_2CoMnO_6, have attracted considerable attention due to their high Curie temperature, T_C, and magnetodielectric properties.[7−9] In both cases, the ferromagnetic (FM) ordering is explained by superexchange interaction between Mn^{4+} and Ni^{2+} or Co^{2+} according to the Goodenough-Kanamori rules,[10] and it is very sensitive to the ordered distribution of cations in the B-sublattice of the DP structure.[11] In the case of LNMO, cationic order gives rise to 180° ferromagnetic interactions between $Ni^{2+}(d^8, t_{2g}^6e_g^2, S = 1)$ and Mn^{4+} $(d^3, t_{2g}^3e_g^0, S = 3/2)$ ions[12] and results in a T_C very close to RT ($T_C \approx 280$ K). Disordering of Ni and Mn ions, and oxygen vacancies may strongly suppress FM superexchange interaction.[13] In fact, cationic disorder reduces the saturation magnetization from 5 μB/f.u. (the maximum expected for the FM contribution of Ni^{2+} and Mn^{4+}) since, according to the Goodenough-Kanamori rules, disorder introduces antiferromagnetic (AF) Mn^{4+}−O−Mn^{4+} and Ni^{2+}−O−Ni^{2+} interactions.[8,15]

In this work we report on the growth and characterization of $La_2Ni_{1-x}Mn_{1+x}O_6$ thin films prepared by RF magnetron sputtering on top (001)-oriented $SrTiO_3$ (STO) substrates. Substrates have been cleaned in an ultrasonic bath with Milli-Q

Received: December 21, 2018
Revised: March 4, 2019
Published: March 15, 2019

Table 1. Chemical Composition and Stoichiometry Ratio of LNMO-δD (140 mTorr) and LNMO-δG (300 mTorr) Samples

P_{O_2} (mTorr)	La (atom %)	Ni (atom %)	Mn (atom %)	O (atom %)	La/Ni + Mn	Ni/Mn	x
140	19.2 ± 0.2	6.0 ± 0.1	14.0 ± 0.1	60.0 ± 0.5	0.96	0.4	0.43
300	20.0 ± 0.1	9.0 ± 0.1	9.0 ± 0.1	60.0 ± 0.2	1.11	1.0	0.0

water and then annealed at 1000 °C in air for 2 h to obtain a clean and smooth surface typical for single TiO_2 termination.[16] Growth conditions, such as temperature, annealing, and oxygen partial pressure, have been optimized to obtain LNMO thin films with M_S and T_C close to the optimum values. However, it is found that Ni/Mn stoichiometric samples always exhibit values of T_C and M_S far from the optimum ones. In contrast, samples with a remarkable Ni deficiency show excellent magnetic properties. We report a detailed study of structural, magnetic, and transport properties of these two characteristic types of samples.

EXPERIMENTAL DETAILS

A series of LNMO samples were grown with oxygen partial pressures ranging from 70 to 300 mTorr and temperatures between 500 and 900 °C. As-grown samples were annealed in-situ at the same temperature for 1 h under high oxygen pressure (420 Torr, see Supporting Information SI1c). The surface quality of samples was characterized by atomic force microscopy (AFM), using a MFP-3D AFM (Asylum Research) in taping mode. Structural characterization was made by means of X-ray diffraction and reflectivity techniques using a X'Pert MRD-Panalytical and a Siemens D5000 diffractometers. The chemical composition and stoichiometry ratio of LNMO thin films were determined by wavelength dispersive spectrometer (WDS) electron probe microanalysis (EPMA) using a CAMECA SX-50 electron microprobe equipped with four wavelength-dispersive X-ray spectrometers. High-resolution transmission electron microscopy (HRTEM) was used to study the microstructure of cross section specimens of LNMO thin films on a FEITecnai G2F20 S-TWIN HR(S)TEM operated at 200 kV. Cross section specimens were prepared by focus ion beam (FIB). The transport properties were measured in a Physical Properties Measurement System (PPMS, Quantum Design) by a four-probe technique. Magnetization measurements were done using a superconducting quantum interferometer device (SQUID, Quantum Design). X-ray absorption spectroscopy (XAS) and X-ray magnetic circular dichroism (XMCD) were investigated at the Ni and Mn $L_{2,3}$ edges in BL29-BOREAS beamline at ALBA Synchrotron Light Source (Barcelona, Spain). The spectra were measured in both the total electron yield (TEY) and total fluorescence yield (TFY) modes, under ultrahigh vacuum conditions (2×10^{-10} mbar). The applied magnetic field (parallel to the X-ray beam) was 4 T.

RESULTS AND DISCUSSION

Previous results corresponding to LNMO/STO thin films prepared by pulsed laser deposition (PLD)[13,17−20] make evident that magnetic properties depend on film thickness and growth conditions. Similarly, samples prepared by RF sputtering, in a broad range of temperatures (500 °C ≤ T ≤ 900 °C) and oxygen pressure (70 mTorr ≤ P_{O_2} ≤ 300 mTorr), exhibit strong dependence on the growth conditions. Samples grown/annealed at high temperature and oxygen pressures above ∼200 mTorr show very deficient magnetic properties with T_C below 150 K. On lowering oxygen pressure (maintaining the same annealing temperature), T_C rises up to ∼225 K and then decreases again (see Supporting Information SI1a). We have also found a non-monotonous dependence of T_C on the deposition temperature (see Supporting Information SI1b). On lowering the growth temperature from 900 to 850 °C, at a partial oxygen pressure of 140 mTorr, T_C increases from T_C ∼160 K to ∼240 K (estimated from inflection point). As a result, the optimal Curie temperature, $T_C \approx 240$ K, has been obtained for samples grown/annealed at 850 °C and at an oxygen partial pressure of 140 mTorr. This sample was labeled as LNMO-δD.

According to previous results reported for LNMO samples prepared by PLD, good FM properties (i.e., $T_C \approx 260$ K and $M_S \approx 5$ μ_B/f.u. at low T) are obtained in samples prepared at higher oxygen pressures, i.e., 300 mTorr,[17] or even 800 mTorr, and temperatures around 750−800 °C,[13,14] with in situ annealing (in 760 Torr of O_2) to promote B site cationic ordering and minimize the oxygen deficiency.[21] In general, for lower oxygen pressures, samples present a low saturation magnetization,[13] with the exception of ref 17 where films prepared under p_{O_2} > 180 mTorr are reported to have $M_S \approx 5$ μ_B/f.u..

These results are in contrast with our own observations, so to clarify the origin of those discrepancies we have carefully analyzed the stoichiometry (using EPMA) of our samples. Results are shown in Supporting Information SI2a. It is found that all the samples present a La:(Ni + Mn) atomic ratio near 1, but the Ni/Mn ratio strongly depends on p_{O_2} used in the growth process. Thus, the actual composition of the samples should be expressed as $La_2Ni_{1-x}Mn_{1+x}O_6$. Samples grown at high pressure present a Ni/Mn ratio close to 1 (and thus good stoichiometry), but at lower pressures samples become Ni-deficient, reaching values of a Ni/Mn ratio of about 0.3 ($x \approx 0.54$, $La_2Ni_{0.46}Mn_{1.54}O_6$). In spite of this remarkable Ni deficiency, samples exhibit excellent FM properties (see Supporting Information SI1a). It must be remarked that Blasco et al. report, for bulk $LaNi_{0.25}Mn_{0.75}O_3$, a FM behavior with T_C = 200 K and M_S = 2.75 μ_B/f.u. (equivalent to 5.5 μ_B/f.u. in double perovskite notation). It is also worth to remark that the same work reports stoichiometric oxygen content when samples were sintered in O-poor atmosphere (Ar). On another hand, a very detailed local study of LNMO films grown by molecular beam epitaxy (at very low oxygen pressure) has shown a spontaneous segregation of the stoichiometric La_2NiMnO_6 into a $La_2Ni_{1-x}Mn_{1+x}O_6$ ($x \approx 0.2$) matrix and NiO inclusions.[22]

Lowering the growth/annealing temperature to 850 °C has little effect on the stoichiometry of the films (see Supporting Information SI2b) which are still Ni deficient. Actually, sample LNMO-δD has a Ni/Mn ratio of 0.40 (x = 0.43) as shown in Table 1. Next, we will focus on two samples prepared by using the same conditions: growth temperature 850 °C and annealing at 850 °C for 60 min, one under 140 mTorr of O_2 pressure (LNMO-δD), and the second under 300 mTorr (LNMO-δG). This second sample has nearly the nominal Ni/Mn = 1 stoichiometry but poor ferromagnetic properties.

XRR curves of nonstoichiometric (LNMO-δD) and stoichiometric (LNMO-δG) samples are depicted in Figure 1a,b, which correspond to the highest and lowest T_C obtained, the fitting to these data (black lines) has been done using XRay utilities library.[23] Thickness values found for both samples are

DOI: 10.1021/acs.cgd.8b01897
Cryst. Growth Des. 2019, 19, 2765−2771

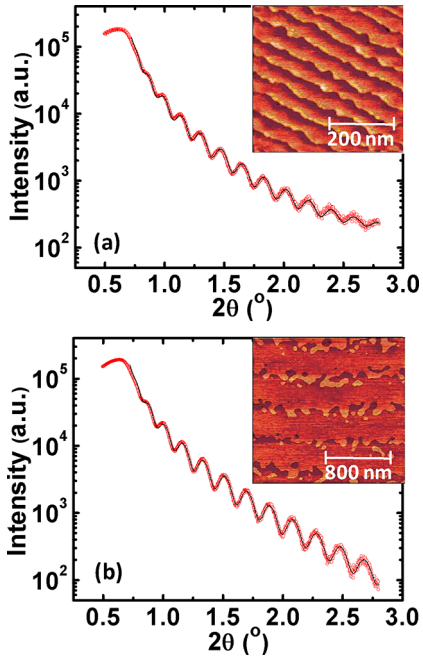

Figure 1. XRR data of (a) LNMO-δD (140 mTorr O_2) and (b) LNMO-δG (300 mTorr O_2) thin films grown on STO(001) substrate, with thickness values of 42 and 44 nm; insets show AFM topography images of a small area of the samples.

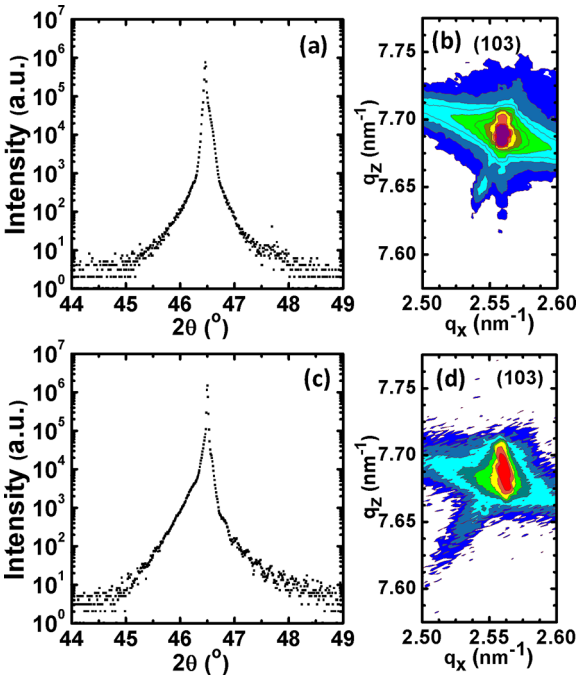

Figure 2. High-resolution $\theta/2\theta$ XRD scans of the (002) reflections for (a) LNMO-δD and (c) LNMO-δG films. Panels (b) and (d) show RSM around (103) reflections for the same samples.

very similar (42 and 44 nm). Inset in Figure 1 shows AFM topography images in tapping mode of both films, topography shows a high quality flat surface with a terrace-steps type morphology. The root-mean-square (rms) value of surface roughness is found to be very small about of 0.2 nm and steps height of about 0.4 nm, corresponding to the perovskite unit cell. Annealing at high oxygen pressures (420 Torr) favors the formation of well-defined terraces mimicking the STO substrate.

In addition, structural properties have been investigated by high resolution $\theta/2\theta$ X-ray diffraction (XRD), Figure 2a,c shows scans around $(002)_{STO}$ reflection using Cu−$K_{\alpha 1}$ monochromatic radiation of LNMO-δD and LNMO-δG samples, respectively. From these $\theta/2\theta$ XRD scans the corresponding out-of-plane lattice parameters are determined: c = 3.895 Å for LNMO-δD and c = 3.908 Å LNMO-δG, which are slightly higher than the pseudocubic perovskite lattice parameter of bulk LNMO, namely, 3.879 Å,[24] and this difference may be caused by the presence of Mn^{3+}. It is also worth mentioning here that Laue fringes can only be seen in LNMO-δG sample but not in LNMO-δD one. Reciprocal space maps, around $(103)_{STO}$ reflection of the same samples, are shown in Figure 2b,d. Measures evidence that films grow fully strained. In fact, for LNMO-δD sample, a small peak coming from the LNMO film can be seen just above the substrate peak. For LNMO-δG sample, both peaks are fully overlapped due to the high similarity between the out-of-plane lattice parameters.

A deeper insight into the microstructural features can be obtained by using high resolution transmission electron microscopy (HRTEM) (see Figure 3a,b. For HRTEM observations in Figure 3a sample LNMO-δD was cut along the (100) direction of STO. HRTEM images show the coexistence of domains with different orientations as can be appreciated in the Fourier transform (FT) of the image. The FT of a large area shows different spots corresponding to the enlargement of the LNMO lattice with respect to STO (LNMO cell parameters are of the type $a \approx b \approx \sqrt{2}a_p$, $c \approx 2a_p$ where a_p is the primitive perovskite cell parameter). These spots can be indexed as (0 k/2 l) (k odd), (0 k l/2) (l odd), and (0 k/2 l/2) (k and l odd) and indicate different orientations of the LNMO cell in the film. This is better illustrated by FT of small regions. For some regions only spots corresponding to (0 k/2 l) (k odd) are found thus in those regions c_{LNMO} is parallel to (010)-STO substrate direction; in other zones only spots of the type (0 k l/2) (l odd) can be seen, which correspond to c_{LNMO} parallel to (001)-STO; and finally a third type of regions where spots of the type (0 k/2 l/2) (k and l odd) are present corresponds to c_{LNMO} parallel to (100)-STO. On the other hand, in Figure 3b sample LNMO-δG was cut along the (110)-STO direction. In this case, the sample is more homogeneous, only one type of spot corresponding to the larger cell of LNMO is observed, and superstructure spots are indexed as (h/2 −h/2 l/2) (h and l odd). This indicates that the orientation of c_{LNMO} axis is parallel to (100) or (010) (in the plane of the film). Therefore, HRTEM observations confirm that domains with in-plane and out-of-plane orientations of c_{LNMO} coexist in LNMO-δD sample, while only in-plane orientation of c_{LNMO} is stabilized for LNMO-δG sample. This multiple orientations of c-axis in LNMO-δD must be related to the absence of Laue fringes in the $\theta/2\theta$ scans.

Zero field cooling-field cooling (ZFC-FC) magnetization curves of both, LNMO-δD and LNMO-δG, samples measured using a field of $H \approx 0.1$ T, are depicted in Figure 4a. This figure evidences the strong dependence of the magnetic behavior on the oxygen pressure during the growth process. $M(T)$ curves of LNMO-δG sample do not show evidence of ferromagnetic ordering. On the other hand, $M(T)$ curves of LNMO-δD display the expected temperature dependence of

DOI: 10.1021/acs.cgd.8b01897
Cryst. Growth Des. 2019, 19, 2765−2771

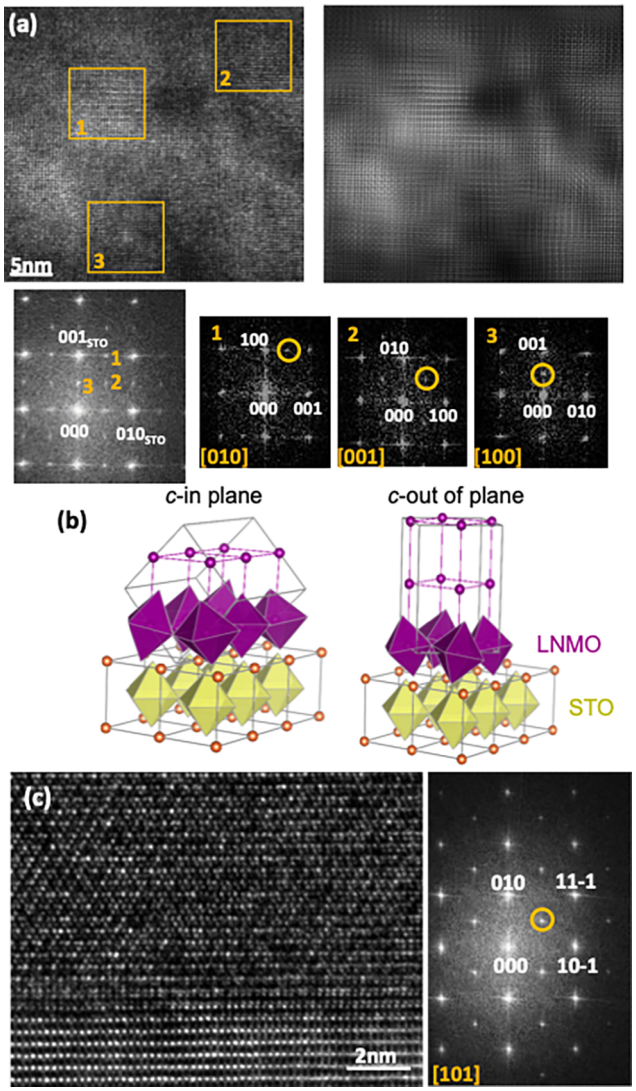

Figure 3. (a) Cross-section HRTEM image of the LNMO-δD (140 mTorr) film viewed along the STO [100] zone axis and corresponding Fourier filtered image emphasizing the strain state of the film and the coexistence of nanodomains with different orientations. Bottom panels show, from left to right, an FFT of the whole image exhibiting superlattice spots at (0 0 l/2), (0 k/2 l/2), and (0 k/2 0) (indexed according to STO orientation), and FFT patterns obtained from windows **1**, **2** and **3**, respectively, revealing the orientations of different nanodomains: In **1** the c-axis of the film is in-plane and parallel to the image, in **2** the c-axis is in-plane and perpendicular to the image, and in **3** it is oriented out-of-plane. In **1**, **2**, and **3**, peaks and zone axes are referred to the pseudocubic unite cell of LNMO. (b) Schematic models for the observed epitaxial relationships. (c) Cross-section HRTEM image and corresponding FFT pattern of the LNMO-δG (300 mTorr) film viewed along the [110] zone axis, exhibiting high crystalline quality and an in-plane orientation of the monoclinic c_{LNMO} axis. The encircled spot corresponds to the (h/2 h/2 −l/2) superlattice. Indices are referred to the pseudocubic unit cell of LNMO.

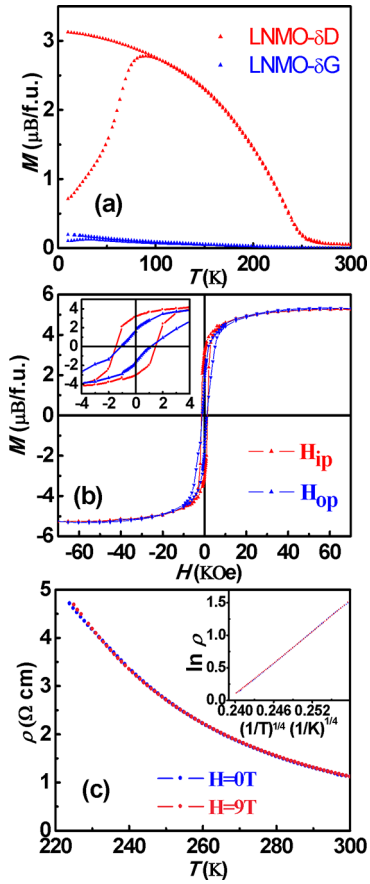

Figure 4. (a) Magnetization measured after ZFC and FC as a function of temperature under an applied field of 1 kOe (in the plane of the film) of LNMO-δD (140 mTorr O_2, red curve) and LNMO-δG (300 mTorr O_2, blue curve). (b) $M(H)$ hysteresis loops of LNMO-δD at 10 K for H applied in-plane and out-of-plane, the inset shows in detail the low field region. (c) Temperature dependent resistivity of LNMO-δD under zero and 9 T magnetic field. Inset, ln ρ vs $(1/T)^{1/4}$.

an FM with no signal of double transition, and a Curie temperature of about 240 K. The field dependence of the magnetization, $M(H)$, after correcting the diamagnetic contribution from substrate and other instrumental contributions,[25] is shown in Figure 4b. $M(H)$ loops corresponding to sample LNMO-δD at T = 10 K exhibit the expected hysteretic behavior with a coercive field of about 1.4 kOe and 1.2 kOe for the field applied in-plane and out-of-plane configurations, respectively. Accordingly, magnetization remanence for the in-plane configuration ($M_r \approx 3.1\ \mu_B$/f.u) is larger than that found for the out-of-plane ($M_r \approx 1.7\ \mu_B$/f.u). A saturation magnetization of $M_s \approx 5.3\ \mu$B/f.u, is found, i.e., somewhat larger than the expected theoretical value (~5 μ_B/f.u.) for perfectly ordered stoichiometric $La_2Ni^{2+}Mn^{4+}O_6$,[26] and also larger than the experimental bulk value (~4.96 μB/f.u.). At this point it is worth mentioning that nonstoichiometry enhances the maximum value achievable for the magnetization for full FM ordering. For the stoichiometry (Ni/Mn ratio) found in our case M_s should be around 5.9 μ_B/f.u., as 2 μ_B/Ni (× 0.57 Ni/f.u.) are attributed to Ni^{2+} and 3.34 μ_B/Mn (× 1.43 Mn/f.u.) to $Mn^{3.66+}$ (as a fraction of Mn^{4+} must reduce to Mn^{3+} to compensate Ni deficiency).

On the other hand, according to Figure 4b the easy magnetization direction lies in the film plane. Although this is the usual behavior in thin films since shape anisotropy tends to place magnetization in plane, the large remanence coercive field of the out-of-plane magnetization curve cannot be understood by considering only shape anisotropy and indicates that magnetocrystalline anisotropy also plays an important role. Furthermore, HRTEM characterization has shown that domains with different crystallographic orientations coexist. Consequently, magnetocrystalline anisotropy would contribute

DOI: 10.1021/acs.cgd.8b01897
Cryst. Growth Des. 2019, 19, 2765−2771

to both in-plane and out-of-plane directions, in accordance with the observed behavior.

Figure 4c shows the temperature and field-dependence of the resistivity of the LNMO-δD film. The measurements show that the resistivity values increase when cooling, thus exhibiting insulating behavior in the whole temperature range. Almost no magnetic field dependence of the resistivity is detected even when crossing T_C (~240 K). The temperature dependence can be well described by using a three-dimensional (3D) variable-range hopping (VRH) model: $\rho(T) = \rho_0 \exp(T_0/T)^{1/4}$, where ρ_0 is the prefactor and T_0 is the characteristic hopping temperature, related to the electron hopping probability, P, of the material.[27] The slope of the curve corresponds to $T_0^{1/4}$, and in this case, we have obtained a value of $T_0 \approx 0.4 \times 10^8$ K, which is similar to the values reported for other transition metal oxides.[28,29]

As mentioned in the introduction, the FM character of La_2NiMnO_6 is understood in terms of the superexchange interactions between Ni^{2+} and Mn^{4+} according to the Goodenough-Kanamori rules. However, the large Ni deficiency found in LNMO-δD sample puts a question mark over this interpretation. To determine the valence states of Ni and Mn ions in Ni-deficient samples, X-ray absorption spectroscopy (XAS) experiments have been carried out in LNMO-δD ($x \approx 0.43$) sample (at two different temperatures: 20 and 300 K). The $L_{2,3}$ ($2p \rightarrow 3d$ transition) XAS spectra, measured by using the TEY technique, corresponding to Mn and Ni are shown in Figure 5a,b. The Ni L_3 edge (see Figure 5b) is overlapped with the La M ($3d_{3/2} \rightarrow 4f$) absorption peak and is hard to analyze. In contrast, the Ni L_2 edge ($\hbar\upsilon \approx 865-875$ eV) absorption peak (shown in the inset) can be easily compared with that of NiO (Ni^{2+}) also shown in the inset. All three edges present a double peak feature that is quite similar to all Ni-divalent compounds and is well understood in terms of a covalent ground state of mainly Ni^{2+} ($3d^8$) character plus an anion-dependent fraction of the $3d^9\underline{L}$ and $3d^{10}\underline{L}$ configurations, where $\underline{L}$ stands for an anion (ligand) hole.[30,32] This double peak is also displayed by L_2 edge of a stoichiometric (and with almost full cationic ordering) sample of La_2NiMnO_6, and very different from the L_2 peak of $PrNiO_3$ and $NdNiO_3$ corresponding to (Ni^{3+}).[31,32] Therefore, we can conclude that the oxidation states of Ni ions in our Ni-deficient sample is 2+. It is worth mentioning that a XANES study in bulk samples of $LaNi_{1-x}Mn_xO_3$ has concluded that for $x \geq 0.5$ the valence of Ni stabilizes to 2+.[33]

In order to determine the valence of Mn, we have also measured the $L_{2,3}$ edges of reference samples $LaMnO_3$ (Mn^{3+}), $La_{0.7}Sr_{0.3}MnO_3$ ($Mn^{3.3+}$), and $CaMnO_3$ (Mn^{4+}). Spectra measured in both TEY and TFY detection modes at room temperature are compared in Figure 5e. A shift of the Mn L_3 peak toward higher energies for all XAS spectra in the series of samples is detected. By comparing L_3 absorption peaks of $LaMnO_3$ at 642.5 eV (Mn^{3+}) and $CaMnO_3$ located at 644.1 eV (Mn^{4+}), with that of LNMO-δD centered between both compounds at 643.5 eV, the valence of the latter can be estimated to be around +3.6. Therefore, assuming a 2+ valence for Ni, and recovering sample stoichiometry values determined by EPMA, a mixed valence of 3.64+ is obtained for Mn. Thus, XAS measurements lead us to conclude that Ni-deficient samples (LNMO-δD) contain a certain quantity of Mn^{3+}, and therefore, Mn must be in a mixed-valence Mn^{3+}/Mn^{4+} oxidation state. For that reason, since Mn^{3+} ions have a larger magnetic moment that Mn^{4+} ones, larger values of the saturation magnetization might be observed in Ni-deficient samples.

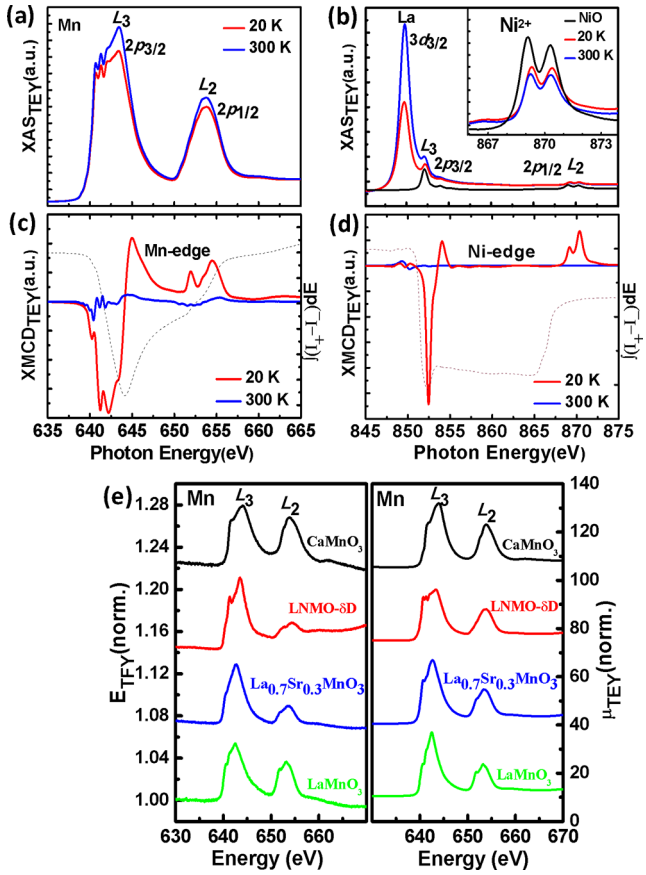

Figure 5. XAS spectra for an epitaxial LNMO-δD thin film. (a) Mn $L_{2,3}$ and (b) Ni $L_{2,3}$, the inset shows the Ni $2p_{1/2}$ absorption peak, absorption spectrum of NiO is also plotted for comparison (black curve). XMCD of (c) Mn $L_{2,3}$ and (d) Ni $L_{2,3}$, measured at 20 K (red curves) and room temperature (RT) (blue curves); the dashed line shows the corresponding integral at 20 K (right axis, note that dashed lines start at zero value). (e) Absorption-corrected FY (left) and TEY (right) Mn $L_{2,3}$ XAS edge of LNMO-δD film compared with reference spectra such as $LaMnO_3$, LSMO, and $CaMnO_3$ at 300 K respectively.

X-ray magnetic circular dichroism (XMCD) has been used to investigate the specific magnetic properties of Mn and Ni ions in the LNMO-δD sample. All the XMCD spectra (see Figure 5c,d) have been normalized to the integrated area of the corresponding XAS spectra.[33] These spectra were measured by the TEY method at 20 K and 300 K. It is found that L_3 absorption peak shows a strong negative XMCD signal at both Ni and the Mn edges, which indicates that the Ni^{2+} and Mn^{4+} ions are aligned ferromagnetically. The XMCD signal nearly disappears at room temperature (above T_C).

In order to extract quantitative information about orbital magnetic moment μ_{orb} and spin magnetic moment μ_{spin} contributions to the magnetic moment of Mn 3d and Ni 3d states, we made use of the so-called sum-rules in the XMCD spectra.[34−36]

$$\mu_L = -\frac{4\left(\int_{L_3} \Delta I(E)\, dE + \int_{L_2} \Delta I(E)\, dE\right)}{3\left(\int_{L_3} I(E)\, dE + \int_{L_2} I(E)\, dE\right)}(10 - N_{3d}) \quad (1)$$

DOI: 10.1021/acs.cgd.8b01897
Cryst. Growth Des. 2019, 19, 2765−2771

$$\mu_S + 7\mu_T = -\frac{2\int_{L_3}\Delta I(E)\,dE - 4\int_{L_2}\Delta I(E)\,dE}{\int_{L_3} I(E)\,dE + \int_{L_2} I(E)\,dE}(10 - N_{3d}) \quad (2)$$

where $\Delta I = I^+ - I^-$; $I = I^+ + I^-$; N_{3d} is the 3d electron occupation number and μ_T is the magnetic-dipole moment (usually negligible for transition metals in octahedral environment). The corresponding integral of the XMCD signal is also depicted in (Figure 5c,d). In the case of Mn ions from the integral of XMCD signal it is found that $\mu_L^{Mn} \approx 0$. In contrast we obtained $\mu_L^{Ni}/\mu_S^{Ni} = 0.32$ at 20 K for Ni. Thus, XMCD study reveals that orbital moment of Ni is not quenched. It is worth mentioning that this orbital contribution is necessary for spin−orbit interactions giving rise to magnetocrystalline anisotropy and reinforces the interpretation that this must be the origin of the magnetic anisotropy evidenced in Figure 4b.

CONCLUSIONS

In summary, we have shown that high-quality epitaxial thin films of the double perovskite LNMO, with Curie temperatures of T_c = 240 K and saturation magnetization of 5.3 μ_B/f.u., can be prepared by using the RF sputtering technique. However, magnetic properties turn out to be strongly dependent on the preparation conditions, particularly on the oxygen partial pressure, p_{O_2}, used during the growth process. Samples prepared at low p_{O_2} (≤140 mTorr) are Ni-deficient with a Ni/Mn ratio of about 0.43, while those prepared at high p_{O_2} (≥300 mTorr) show the expected Ni/Mn ≈ 1 ratio. However, stoichiometric samples show poor ferromagnetic properties, i.e., low T_c and low saturation magnetization. In contrast, nonstoichiometric samples exhibit high $T_c \approx 240$ K and high saturation magnetization of $M_s \approx 5.3$ μ_B/f.u. Assuming that FM ordering in the double perovskite structure comes from superexchange interactions between Ni^{2+} and Mn^{4+}, according to the Goodenough-Kanamori rules, the values of T_c and M_s obtained for stoichiometric samples clearly indicate that Ni/Mn cationic ordering in the B-sublattice is absent. On the other hand, XAS measurements allow concluding that Ni ions are stabilized as Ni^{2+} even in nonstoichiometric samples. Additionally, XAS measurements in nonstoichiometric samples also demonstrate that Mn ions are in a mixed-valence Mn^{3+-4+} state with an effective valence of +3.6. However, samples exhibit insulating behavior, and therefore double-exchange interaction cannot be invoked to explain the observed FM ordering. So, to explain the excellent magnetic properties found in Ni-deficient samples some kind of cationic ordering between Ni^{2+}, Mn^{3+}, and Mn^{4+} in the B sublattice has to be assumed, and thus, the question of whether a Ni deficiency can favor Ni/Mn ordering arises. On the other hand, our XMCD measurements show that the contribution of the orbital moment to the magnetic moment of Mn ions is negligible, but for Ni ions it is quite important, $\mu_L^{Ni}/\mu_S^{Ni} = 0.32$, thus allowing us to conclude that magnetic anisotropy observed in the magnetic measurements ($M(H)$ loops) is of magnetocrystalline origin.

ASSOCIATED CONTENT

Supporting Information

The Supporting Information is available free of charge on the ACS Publications website at DOI: 10.1021/acs.cgd.8b01897.

Additional $M(T)$ curves and stoichiometry of the LNMO films (PDF)

AUTHOR INFORMATION

Corresponding Author

*E-mail: mbernal@icmab.es. Telephone: +34 935 801 853.

ORCID

Carlos Frontera: 0000-0002-0091-4756

Benjamín Martínez: 0000-0001-9879-7748

Notes

The authors declare no competing financial interest.

ACKNOWLEDGMENTS

M.B.-S., Ll.B., F.S., B.B., C.F., B.M., and A.P. acknowledge financial support from the Spanish Ministry of Economy and Competitiveness through the "Severo Ochoa" Programme for Centres of Excellence in R&D (SEV-2015-0496), and Project MAT2015-71664-R. This work has received funding from the European Union's Horizon 2020 Research and Innovation Programme under the Marie Sklodowska-Curie Grant Agreement No. 645658 (DAFNEOX Project). Z.K. acknowledge the support of the Serbian Ministry of Education, Science and Technological Development (III45018). Authors thank ALBA synchrotron (Spain) for the provision of beamtime.

REFERENCES

(1) Bibes, M.; Villegas, J. E.; Barthélémy, A. Ultrathin oxide films and interfaces for electronics and spintronics. *Adv. Phys.* **2011**, *60*, 5.

(2) Žutic, I.; Fabian, J.; Das Sarma, S. Spintronics: Fundamentals and applications. *Rev. Mod. Phys.* **2004**, *76*, 323.

(3) Moodera, J. S.; Gallagher, E. F.; Robinson, K.; Nowak, J. Optimum tunnel barrier in ferromagnetic−insulator−ferromagnetic tunneling structures. *Appl. Phys. Lett.* **1997**, *70*, 3050.

(4) Itoh, H.; Ozeki, J.; Inoue, J. Electronic structure and spin-filter effect of ferromagnetic insulators with double perovskite structure. *J. Magn. Magn. Mater.* **2007**, *310*, 1994−1996.

(5) Li, P.; Xia, C.; Zhu, Z.; Wen, Y.; Zhang, Q.; Alshareef, H. N.; Zhang, X.-X. Ultrathin Epitaxial Ferromagnetic γ-Fe 2 O 3 Layer as High Effi ciency Spin Filtering Materials for Spintronics Device Based on Semiconductors. *Adv. Funct. Mater.* **2016**, *26*, 5679.

(6) López-Mir, L.; Frontera, C.; Aramberri, H.; Bouzehouane, K.; Cisneros-Fernández, J.; Bozzo, B.; Balcells, L.; Martínez, B. Anisotropic sensor and memory device with a ferromagnetic tunnel barrier as the only magnetic element. *Sci. Rep.* **2018**, *8*, 861.

(7) Dass, R. I.; Goodenough, J. B. Multiple magnetic phases of La2CoMnO$_{6-\delta}$ ($0 \le \delta \le 0.05$). *Phys. Rev. B: Condens. Matter Mater. Phys.* **2003**, *67*, 014401.

(8) Dass, R. I.; Yan, J.-Q.; Goodenough, J. B. Oxygen stoichiometry, ferromagnetism, and transport properties of La2-xNiMnO$_{6+\delta}$. *Phys. Rev. B: Condens. Matter Mater. Phys.* **2003**, *68*, 064415.

(9) Devi Chandrasekhar, K.; Das, A. K.; Mitra, C.; Venimadhav, A. The extrinsic origin of the magnetodielectric effect in the double perovskite La2NiMnO$_6$. *J. Phys.: Condens. Matter* **2012**, *24*, 495901.

(10) Goodenough, J. B. An interpretation of the magnetic properties of the perovskite-type mixed crystals La$_{1-x}$Sr$_x$CoO$_{3-\lambda}$. *J. Phys. Chem. Solids* **1958**, *6*, 287.

(11) Goodenough, J. B.; Wold, A.; Arnott, R. J.; Menyuk, N. Relationship Between Crystal Symmetry and Magnetic Properties of Ionic Compounds Containing. *Phys. Rev.* **1961**, *124*, 373.

(12) Hashisaka, M.; Kan, D.; Masuno, A.; Takano, M.; Shimakawa, Y.; Terashima, T.; Mibu, K. Epitaxial growth of ferromagnetic with ordered double-perovskite structure. *Appl. Phys. Lett.* **2006**, *89*, 032504.

(13) Guo, H. Z.; Burgess, J.; Ada, E.; Street, S.; Gupta, A.; Iliev, M. N.; Kellock, A. J.; Magen, C.; Varela, M.; Pennycook, S. J. Influence of

DOI: 10.1021/acs.cgd.8b01897
Cryst. Growth Des. 2019, 19, 2765−2771

defects on structural and magnetic properties of multifunctional La2NiMnO$_6$ thin films. *Phys. Rev. B: Condens. Matter Mater. Phys.* **2008**, *77*, 174423.
(14) Truong, K. D.; Singh, M. P.; Jandl, S.; Fournier, P. Influence of Ni/Mn cation order on the spin-phonon coupling in multifunctional La2NiMnO$_6$ epitaxial films by polarized Raman spectroscopy. *Phys. Rev. B: Condens. Matter Mater. Phys.* **2009**, *80*, 134424.
(15) Zhao, S.; Shi, L.; Zhou, S.; Zhao, J.; Yang, H.; Guo, Y. Size-dependent magnetic properties and Raman spectra of La2NiMnO$_6$ nanoparticles. *J. Appl. Phys.* **2009**, *106*, 123901.
(16) Konstantinović, Z.; Santiso, J.; Colson, D.; Forget, A.; Balcells, Ll.; Martínez, B. Self-organization processes in highly epitaxial La2/3Sr1/3MnO3 thin films grown on SrTiO3 (001) substrates. *J. Appl. Phys.* **2009**, *105*, 063919.
(17) Hashisaka, M.; Kan, D.; Masuno, A.; Takano, M.; Shimakawa, Y.; Terashima, T.; Mibu, K. Epitaxial growth of ferromagnetic La$_2$NiMnO$_6$ with ordered double-perovskite structure. *Appl. Phys. Lett.* **2006**, *89*, 032504.
(18) Guo, H.; Burgess, J.; Street, S.; Gupta, A.; Calvarese, T. G.; Subramanian, M. A. Growth of epitaxial thin films of the ordered double perovskite La2NiMnO$_6$ on different substrates. *Appl. Phys. Lett.* **2006**, *89*, 022509.
(19) Iliev, M. N.; Guo, H.; Gupta, A. Raman spectroscopy evidence of strong spin-phonon coupling in epitaxial thin films of the double perovskite La2NiMnO$_6$. *Appl. Phys. Lett.* **2007**, *90*, 151914.
(20) Sakurai, Y.; Ohkubo, I.; Matsumoto, Y.; Koinuma, H.; Oshima, M. Influence of substrates on epitaxial growth of B-site-ordered perovskite La$_2$NiMnO$_6$ thin films. *J. Appl. Phys.* **2011**, *110*, 063913.
(21) Guo, H.; Burgess, J.; Street, S.; Gupta, A.; Calvarese, T. G.; Subramanian, M. A. Growth of epitaxial thin films of the ordered double peroskite La2NiMnO$_6$ on different substrates. *Appl. Phys. Lett.* **2006**, *89*, 022509.
(22) Spurgeon, S. R.; Du, Y.; Droubay, T.; Devaraj, A.; Sang, X.; Longo, P.; Yan, P.; Kotula, P. G.; Shutthanandan, V.; Bowden, M. E.; LeBeau, J. M.; Wang, C.; Sushko, P. V.; Chambers, S. A. Competing pathways fro nucleation of the double perovskite structure in the epitaxial synthesis of La$_2$MnNiO$_6$. *Chem. Mater.* **2016**, *28*, 3814−3822.
(23) Kriegner, D.; Wintersberger, E.; Stangl, J. Xrayutilities: a versatile tool for reciprocal space conversion of scattering data recorded with linear and area detectors. *J. Appl. Crystallogr.* **2013**, *46*, 1162−1170.
(24) Guo, H.; Burgess, J.; Street, S.; Gupta, A.; Calvarese, T. G.; Subramanian, M. A. Growth of epitaxial thin films of the ordered double perovskite La2NiMnO$_6$ on different substrates. *Appl. Phys. Lett.* **2006**, *89*, 022509.
(25) Stamenov, P.; Coey, J. M. D. Sample size, position, and structure effects on magnetization measurements using second-order gradiometer pickup coils. *Rev. Sci. Instrum.* **2006**, *77*, 015106.
(26) Rogado, N. S.; Li, J.; Sleight, A. W.; Subramanian, M. A. Magnetocapacitance and Magnetoresistance Near Room Temperature in a Ferromagnetic Semiconductor: La2NiMnO$_6$ Adv. *Adv. Mater.* **2005**, *17*, 2225−2227.
(27) Guo, Y.; Shi, L.; Zhou, S.; Zhao, J.; Liu, W. Near room-temperature magnetoresistance effect in double perovskite La$_2$NiMnO$_6$. *Appl. Phys. Lett.* **2013**, *102*, 222401.
(28) Renner, B.; Lunkenheimer, P.; Schetter, M.; Loidl, A.; Reller, A.; Ebbinghaus, S. G. Dielectric behavior of copper tantalum oxide. *J. Appl. Phys.* **2004**, *96*, 4400.
(29) Lin, Y. Q.; Chen, X. M.; Liu, X. Q. Relaxor-like dielectric behavior in La$_2$NiMnO$_6$ double perovskite ceramics. *Solid State Commun.* **2009**, *149*, 784−787.
(30) Medarde, M.; Fontaine, A.; Garcia-Munoz, J. L.; Rodriguez-Carvajal, J.; De Santis, M.; Sacchi, M.; Rossi, G.; Lacorre, P. RNio$_3$ perovskites (R = Pr,Nd): Nickel valence and the metal-insulator transition investigated by x-ray-absorption spectroscopy. *Phys. Rev. B: Condens. Matter Mater. Phys.* **1992**, *46*, 14975.
(31) Guo, H.; Gupta, A.; Varela, M.; Pennycook, S.; Zhang, J. Local valence and magnetic characteristics of La$_2$NiMnO$_6$. *Phys. Rev. B: Condens. Matter Mater. Phys.* **2009**, *79*, 172402.
(32) Sánchez, M. C.; García, J.; Blasco, J.; Subías, G.; Perez-Cacho, J. Local electronic and geometrical structure of LaNi$_{1-x}$Mn$_x$O$_{3+\delta}$ perovskites determined by x-ray-absorption spectroscopy. *Phys. Rev. B: Condens. Matter Mater. Phys.* **2002**, *65*, 144409.
(33) Kang, J.-S.; Lee, S. M.; Kim, D. H.; Kolesnik, S.; Dabrowski, B.; Park, B.-G.; Kim, J.-Y.; Lee, J.; Kim, B.; Min, B. I. Temperaturedependent magnetic circular dichroism study of ferromagnetic double perovskite La$_2$MnNiO$_6$. *J. Appl. Phys.* **2010**, *107*, 09D721.
(34) Guo, H.; Gupta, A.; Varela, M.; Pennycook, S.; Zhang, J. Local valence and magnetic characteristics of La$_2$NiMnO$_6$. *Phys. Rev. B: Condens. Matter Mater. Phys.* **2009**, *79*, 172402.
(35) Carra, P.; Thole, B. T.; Altarelli, M.; Wang, X. X-Ray Circular Dichroism and Local Magnetic Fields. *Phys. Rev. Lett.* **1993**, *70*, 694.
(36) Thole, B. T.; Carra, P.; Sette, F.; van der Laan, G. X-Ray Circular Dichroism as a Probe of Orbital Magnetization. *Phys. Rev. Lett.* **1992**, *68*, 1943.

DOI: 10.1021/acs.cgd.8b01897
Cryst. Growth Des. 2019, 19, 2765−2771